Journal of Applied Physics

Argon Metastable Density and Temperature of a 43 GHz Microplasma

Rafael Navarro and Jeffrey Hopwood

Electrical and Computer Engineering Department, Tufts University, Medford, 02155, Massachusetts, USA

E-mail: hopwood@ece.tufts.edu

Received xxxxxx
Accepted for publication xxxxxx
Published xxxxxx

Abstract

The argon ($1s_5$) metastable density and translational gas temperature are experimentally measured using laser diode absorption spectroscopy within a 43 GHz microplasma. The plasma is initiated and sustained within a photonic crystal constructed from a rectangular array of alumina rods, each 1 mm in diameter. This configuration generates a stable microplasma from 10 – 600 Torr using millimeter wave power from 100 mW to 1200 mW. The metastable density is the order of 10^{18} m^{-3} at low pressure. The Ar($1s_5$) density decreases to undetectable levels with increasing pressure and wave power, however. The gas temperature is extracted from the Lorentzian line shape of the absorption profile at 811.53 nm. The gas temperature increases from approximately 400 K at low pressure to 2000 K at 320 Torr (427 mbar, $4.27x10^4$ Pa). These data are compared with previous results and suggest that the microplasma has a dense core of electrons that depletes the metastable density at high gas pressure and wave power.

1. Introduction

Yablonovitch and John [1], [2] conceived controlling the radiative properties of materials by using photons or affecting photon localization by varying the refractive index of materials [3]–[6]. Since then photonic crystals (PhC) have been designed and created, for basic studies and for different applications [7]–[10]. The diverse frequency ranges include microwaves and millimeter waves (MMW), but also optical radiation bands.

In its pristine state, a photonic crystal consists of a periodic lattice, such as dielectric rods, which prevent a wave from being propagated through it in a specific frequency range [11], [12]. This frequency range is well-known as the photonic bandgap [1], [2], [7], [11]–[16]. If this periodic lattice is modified by subtracting a dielectric element from a strategic region, a narrow bandpass can appear within this photonic bandgap [11], [17], [18]. The bandpass is due to a resonance and results in intensifying the electric field inside this volume. Alternately, if multiple dielectric elements are deleted from the PhC, the path formed by these defects can be exploited as a waveguide [17], [19] for controlling the signal direction.

A PhC can gain useful dynamic properties by inserting a plasma. Plasma exhibits interesting electromagnetic characteristics such as a negative permittivity [20], [21]. It has been the object of study for different research work, where its excitation source signal varies from DC, RF waves, microwaves and MMW.

In the RF domain, an inductively or capacitively coupled plasma is typically used at 13.56 MHz for surface treatments and thin film deposition. Recently these plasmas have been used in combination with metamaterial structures (composed of split ring resonators, SRRs) for understanding the effects of a low pressure plasma on resonance frequency [22], and for verifying wave propagation through a double negative

medium (DNM) [23]. In the microwave domain, these same metamaterial structures have also been used for creating microplasmas [24], [25] at the gap in each unit cell of the structure composed by SRRs. On the same principle, plasmas have been created in combination with these metamaterial structures for trying to exceed the electron plasma frequency created by a 1.5 GHz [26] and 2.45 GHz source [27].

Recently in this category and more specifically related with the research line in this paper, some PhC devices (or electromagnetic band gap (EBG)) were studied. The plasma switches or tunes the peak of the resonance in a PhC filter [28], acts as the lattice elements of the entire structure [29], [30], or restores a deleted rod element in a vacancy defect [31] in a square 2D PhC with less than 1000 mW as sustaining power. The latter was modeled [32] to be ignited solely by the incident wave. The plasma is modeled to have an electron density with an order of magnitude of 10^{18} m^{-3} in low pressure argon as evidenced in [31].

In the MMW domain on the same research line, low-frequency discharges are found to act as the lattice elements in a square 2D PhC for the 70-75 GHz range [33] and 120-170 GHz range [34], or to restore a missing rod element in a vacancy defect [35] into a hexagonal 2D PhC configuration for a 27 GHz signal. More recently, into the same square 2D PhC configuration as mentioned in [31], an argon microplasma was created in the vacancy defect by an incident wave signal at 43 GHz [36] and sustained with less than 1000 mW. In this configuration the electron density was found to have an order of magnitude of 10^{20} m^{-3} as reported in [37]. Other studies have been made by involving this same PhC and highlighting more characteristics and potential applications [38], [39].

As the electromagnetic wave frequency range increases, the interaction with plasmas created by the EM signal is less understood, so there is interest [40] in investigating the plasma behavior, especially at the THz band [41]. PhCs offer a good choice to achieve and study this interaction, since the PhC functions into the optical bands and has the potentiality of concentrating wave energy into the vacancy defect volume. Some models have been created for predicting the behavior of the plasma in the low THz range [42]–[44]; however, the electron density predicted by these three models diverges as the frequency exceeds 10 GHz. Due to this disagreement, it is important to develop an experimental understanding of plasma parameters at higher frequencies such as electron density, metastable density and gas temperature. These data may help the models to better predict the plasma behavior into the THz band.

In order to collect data to validate the models before mentioned, Kim, et al. [37] report the electron density and gas temperature of an argon microplasma in a vacancy defect in a square 2D PhC configuration at 43 GHz. To diagnose these microplasmas becomes challenging due the small size on the one hand, and the very small confining structure of the PhC that obscures access to the plasma on the other hand. An alternative method for measuring the electron density is that explained by Kim and Hopwood in [39] where MMW spectroscopic measurements of a microplasma were made. In that report, the plasma is found to have an intense central core on the order of 100-200 μm that is surrounded by a weaker diffusion region on the order of 1-2 mm.

The next goal is to estimate the metastable density generated by the 43 GHz plasma. The metastable argon atoms are precursors to ions and free electrons in the two-step ionization process and play a crucial role in plasma formation. For this purpose, a diode laser absorption spectroscopy technique is implemented similar to that reported by Sadeghi [45] and long used for this purpose in different works [46]–[50].

Therefore, and unlike previous work [37], this paper is focused on measuring the Ar($1s_5$) metastable density using the $2p_9$-$1s_5$ electronic transition. In addition, the gas temperature of argon is also found from the line shape deduced from this diode laser absorption spectroscopy technique. In both cases, the diagnostic is specifically probing the high-density central core of the microplasma where the ionization is most intense.

This paper is organized as follows: In Section 2, the experimental configuration is described for the PhC, MMW setup and optical setup. In Section 3, the results are presented, including the line-integrated metastable density, the broadening of the Voigt profile, and an approximation of the gas temperature. These results are interpreted in Section 4.

2. Experimental configuration

2.1 Photonic crystal configuration

This experiment is based on previous reports which generate a microplasma at 43 GHz [36]–[39]. Hence, the physical parameters in this PhC are the same used in previous work, but they are briefly restated here for convenience. The PhC is composed of an 11 × 7 square lattice of alumina rod elements, which are 1 mm in diameter, spaced by 2.8 mm with a height of 2.85 mm, and encapsulated in a copper frame. These rods (CoorsTek, AD-998) have a relative permittivity of $\varepsilon_r = 9.8$ with dielectric loss tangent of $\delta < 0.0001$ at 1 MHz. To concentrate the incident wave's electric field as much as possible in the center of the PhC and thus create the plasma, a vacancy defect was created by removing the central rod as shown in the left side of Fig. 1.

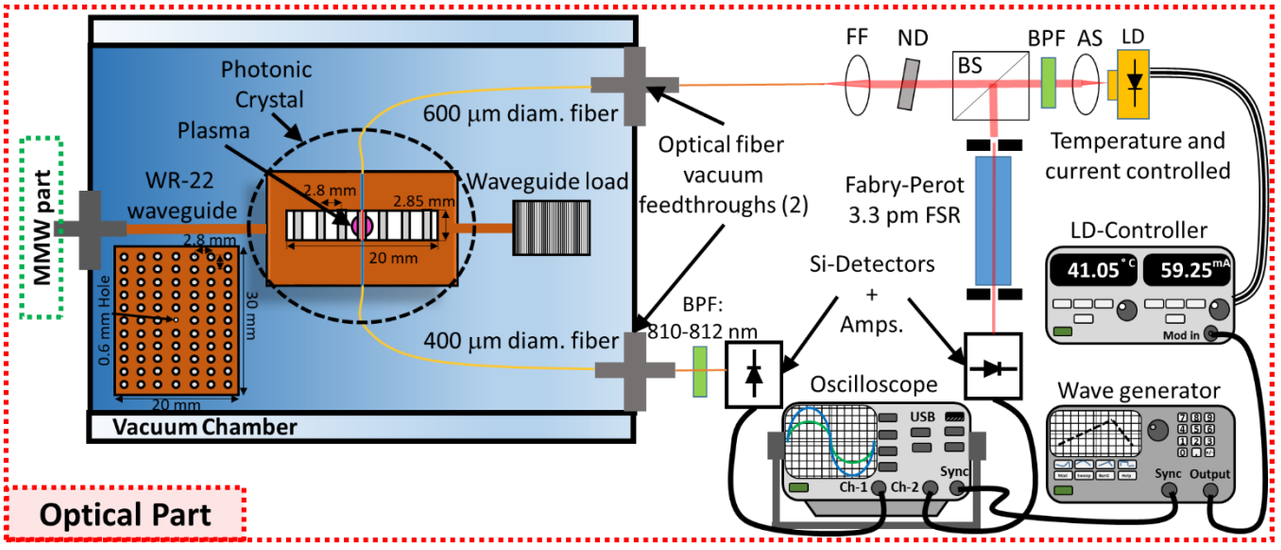

Fig. 1. Schematic of the experimental setup including the optical part (laser diode absorption) and the MMW photonic crystal within a vacuum chamber. The millimeter wave generation is described separately in Figure 2.

This PhC was located in a vacuum chamber evacuated using an oil-lubricated vacuum pump with a base pressure of 10 mTorr. The pressure was measured by a piezo transducer gauge (MKS, 902B). The chamber was then backfilled with argon gas (99.99%) at a pressure near 40 Torr to generate the initial plasma by using a continuous MMW power of 3 W for all experiments.

Laser light was passed through the center of the plasma using two holes. On the top plate of the PhC is a 650 μm hole that accommodates a 600 μm optical fiber connected to a laser diode (LD) nominally operating at 811.53 nm wavelength. In the bottom plate of the PhC is a 450 μm hole that positions a 400 μm optical fiber to receive the laser signal after traversing and being partially absorbed by the plasma. Two optical fiber vacuum feedthroughs permit the passage of the fibers from the exterior to interior of the vacuum chamber.

To determine if the optical access holes caused significant changes in the PhC behavior, a frequency-domain electromagnetic simulation in ANSYS EM19.2, HFSS® was used. Though the modeled resonance frequency shifted upward (15 MHz) and the magnitude of the electric field decreased because of the holes, the maximum electric field was found to be 168 kV/m at 1000 mW. This field is above of the minimum breakdown threshold at a pressure of 30 Torr (70 kV/m) according to Raizer theory [51]. This simulation was confirmed by experimental observation of gas breakdown and stable plasma formation.

2.2 Experimental millimeter wave setup

This section describes the generation and measurement of the incoming 43 GHz electromagnetic wave. A microwave signal of 5 dBm at 10.917 GHz from the signal generator (Keysight, N5183A) is multiplied by a 4×-active multiplier (Millitech, AMC-22). After being multiplied, the MMW signal (43.668 GHz) is increased by the WR-22 waveguide amplifier (Millitech, AMP-22-40060) up to 3 W by manually varying an attenuator as show in the Fig. 2. The amplified wave enters a bidirectional coupler (DC, Millitech, CL4-22, −20 dB) where two power sensors (Keysight, N8487A) were connected to the power meter (Keysight, E8487A) to measure the forward (P_{for}) and reflected (P_{ref}).

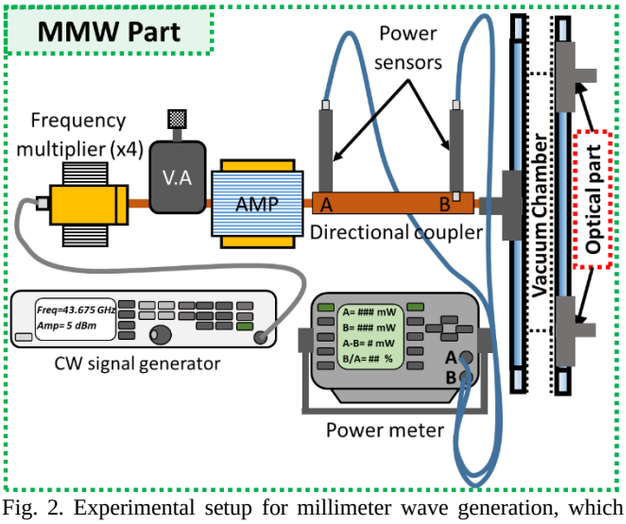

Fig. 2. Experimental setup for millimeter wave generation, which enters the vacuum chamber through a sealed WR-22 waveguide. (Figure 1 describes the optical components and PhC.)

Without plasma, P_{ref} was less than 1% of P_{for}, but in the presence of plasma, P_{ref} increases up to 45%, depending on the electron density (n_e) in the plasma. Hence, the net power

is $P_{net} = P_{for} - P_{ref}$ in the PhC. In absence of the plasma, the PhC is nearly transparent and the transmitted power (P_{tr}) should be almost the same as P_{net}, taking into account the losses in the copper and the dielectric rod elements; however, in the presence of plasma, these losses increase, resulting in a P_{tr} lower than P_{net} due to an absorption power (P_{abs}) in the plasma, hence $P_{net} = P_{tr} + P_{abs}$. This P_{tr} exits the PhC through a WR-22 rectangular cut-out and is absorbed by a waveguide load as shown in Fig. 1.

2.3 Experimental optical setup

A laser diode (LD, Thorlabs L811P010) was mounted on a thermoelectric temperature controller (Thorlabs, TCLDM9) and tuned to 811.53 nm by adjusting the diode laser current to 64 mA at a temperature of 41 °C as shown in the right side of Fig. 1. To produce 811.53 nm, the lasing wavelength was measured by an optical emission spectrometer (Ocean Optics USB2000+) and simultaneously compared to optical emission from the argon plasma while adjusting the LD temperature. Once the center wavelength is established, the laser wavelength is scanned through the linewidth of the argon metastable state by modulating the laser drive current. A 5 Hz, 200 mV signal generator connected to the LD controller provides ±50 pm of wavelength modulation around 811.53 nm.

Since diodes were used in the free running mode (without optical feedback), the available lasing wavelengths are discontinuous, changing between single and multi-mode operations with changes in the case temperature and diode current. To assure laser operation in a single mode, a Fabry-Perot interferometer (FSR=1.5 GHz, finesse >200, resolution <7.5 MHz, Thorlabs, SA200-7A) was used and connected to the laser path by a beam splitter (BS). The intense plasma emission also coupled backward into the laser, causing mode hopping. To alleviate this problem a bandpass filter (BPF, 810 nm, Δλ= 10 nm) was inserted into the path, allowing only the wavelengths coming from the plasma in the 805-815 nm range to strike the LD, thus extending the free running single-mode operation.

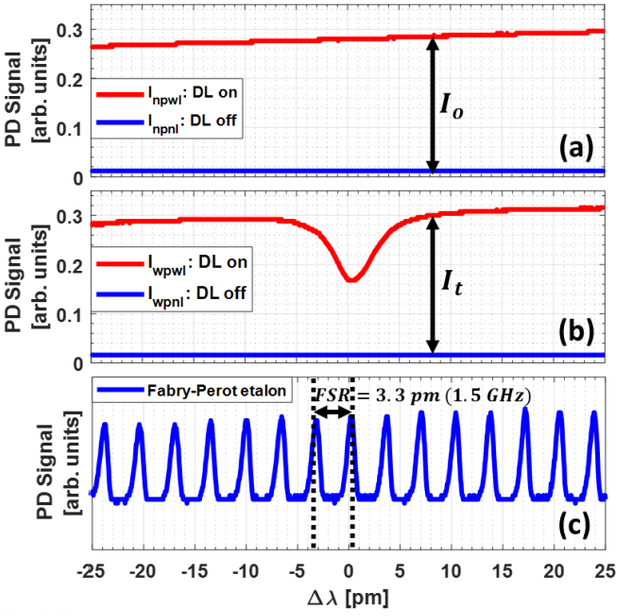

Fig. 3 Typical experimental absorption data (a) without and (b) with plasma. (c) Fabry-Perot etalon calibration signal for the 811.53 nm transition in argon (conditions: 80 Torr and 1000 mW).

An aspheric lens (AS, Thorlabs, C330TME-B) collimated and aligned the diode laser through the optical path. A neutral density (ND) was selected to attenuate the laser intensity until no bleaching of the plasma was observed. The laser was focused onto a 600 μm diameter fiber using a Thorlabs PAF2S-15B fiber focuser (FF). The fiber enters the chamber and passes laser light through the PhC and plasma. The partially-absorbed laser light is collected by a second fiber and exits the vacuum chamber. Plasma emissions outside the wavelength of the laser are filtered by a second bandpass filter. The filtered laser signal is sensed by a diode detector, amplified and measured using a Tektronix TDS2024C oscilloscope. Electrical noise is filtered by averaging 128 scans of the laser per measurement.

To determine the absorption of laser light by the metastable argon atoms in the plasma, one must obtain the incident laser intensity ($I_0 = I_{npwl} - I_{npnl}$) and transmitted laser intensity $I_t = I_{wpwl} - I_{wpnl}$, as a function of wavelength. Four modes were measured:

I_{wpwl} : plasma on, laser on
I_{wpnl} : plasma on, laser off
I_{npwl} : plasma off, laser on
I_{npnl} : plasma off, laser off

As shown in Fig. 3, a typical experimental result at 80 Torr and 100 mW is presented where $\Delta\lambda = 0$ represents $\lambda_0 =$ 811.53 nm as the central value. The absorption linewidth was

calibrated by the appearance of the periodic interference peaks of the laser signal by using the Fabry-Perot etalon as shown in Fig. 3c.

3. Results

When the diode laser absorption technique is implemented, one can assess information about the line-integrated excited-state densities and the gas temperature in the microplasma. In this section the plasma properties related to this technique are addressed and described.

3.1 Metastable density

Photons from the tuned laser are absorbed by the argon $1s_5$ metastable state. The amount of absorption is used to extract the metastable density. According to the Beer-Lambert law, the transmitted light intensity (I_t) after plasma absorption depends on the incident light intensity (I_0) as follows:

$$I_t(\lambda) = I_0(\lambda)e^{(-k(\lambda)l)} \quad (1)$$

$$k(\lambda)l = ln\left(\frac{I_0(\lambda)}{I_t(\lambda)}\right) \quad (2)$$

Where the product $k(\lambda)l$, composed of the absorption coefficient $k(\lambda)$ in [m^{-1}] and the absorption length l in [m], is well-known as the optical depth. Then the line-integrated density of the absorbing species ($N_i l$) is given by [45], [46], [48], [52]:

$$N_i l = \frac{8\pi g_i c}{\lambda_0^4 g_k A_{ki}} \int k(\lambda) l d\lambda \quad (3)$$

Here $N_i l$ is in [m^{-2}], c is the speed of the light in [m/s] and the subscripts i and k reference the lower and upper energy levels of the transition at the wavelength λ_0 in [m], respectively. The constants g_i and g_k are the degeneracies of these states and A_{ki} is the spontaneous emission probability (in s^{-1}). The set of values for these parameters [48] are presented in the Table I.

Table I. Values for line-integrated density parameters [48]

λ_0 (nm)	Transition Low/High	A_{ki} (s^{-1})	g_i/g_k	$\frac{8\pi g_i c}{\lambda_0^4 g_k A_{ki}}$
811.53	1_{S5}-$2p_9$	3.3×10^7	5/7	3.76×10^{26}

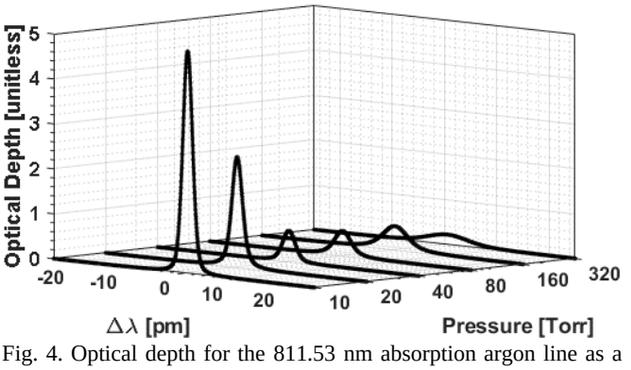

Fig. 4. Optical depth for the 811.53 nm absorption argon line as a function of pressure for a net power of 1000 mW. Curves obtained by using the Voigt-fit to the experimental data.

From the results presented in Fig. 3, we can obtain I_0 and I_t to calculate the optical depth. Fig. 4 shows the optical depth as a function of $\Delta\lambda$. Computing the area under the curve for each pressure, it is then possible to get the line-integrated density using Eq. 3, which is plotted in Fig 5 and Fig. 6.

In Fig. 5, we compare the line-integrated Ar($1s_5$) density from a diffuse low pressure case (10 Torr, 13.3 mbar) with a constricted high pressure plasma (320 Torr, 427 mbar). The connecting lines serve solely to guide the eye. At low pressures, the electron temperature is known to be higher, and therefore the production of excited states is faster. The upward trend of line-integrated density is consistent with increased plasma power and expansion of the plasma's length. The high pressure case appears to produce many fewer metastables, but the plasma length is also shorter. The variation of plasma length along the laser path is addressed in the next section. Most interesting is the counter-intuitive decrease in metastable atoms as the power exceeds 600 mW.

Because metastable density is determined by the integration of the optical depth, the experimental errors are small and comparable to the markers on the plots. However, the plasma may not be 100% consistent from run-to-run, and this is the origin of some variation in the results seen in Fig. 5. Across multiple measurements the trends presented in this manuscript are reproducible.

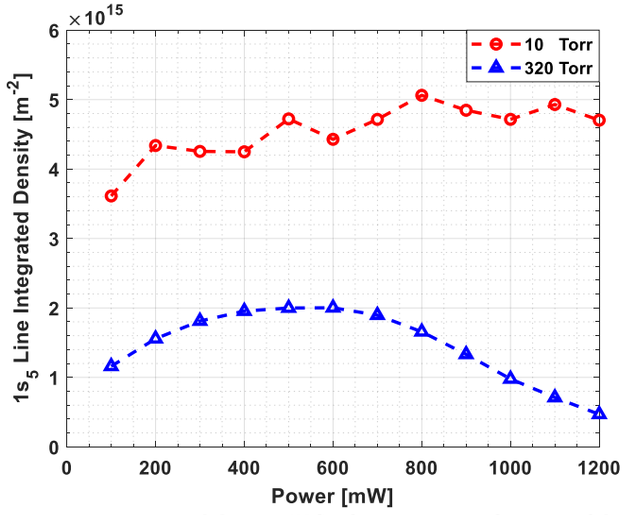

Fig. 5. Line-integrated density ($N_i l$) of argon $1s_5$ as a function of the net power, for a low (red curve) and high (blue curve) pressure (10 and 320 Torr).

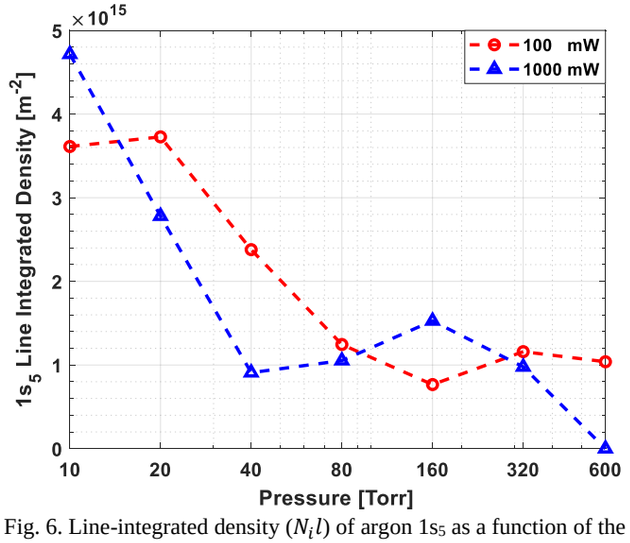

Fig. 6. Line-integrated density ($N_i l$) of argon $1s_5$ as a function of the pressure, for a low (red curve) and high (blue curve) net power (100 mW and 1000 mW).

Because the laser passes through only the central 400 μm of the plasma, only the core of the microplasma is probed. The depletion of metastable argon in this dense central region is addressed in the Discussion section.

In Fig. 6, the cumulative metastable density along the laser path shows a general decrease as the argon pressure approaches one atmosphere. The detailed behavior of the plasma as it transitions from diffuse to constricted is complex and not yet well understood. There is only a weak dependency on the net wave power. The most remarkable observation is the disappearance of laser absorption by metastables in the case of high power (1000 mW) and high pressure (600 Torr, 800 mbar). The optical depth of the plasma was zero within the limits of the experiment, so we report the line-integrated density as zero. Although, physically, one could argue that the density cannot be zero, it is below the detection limit of the experiment.

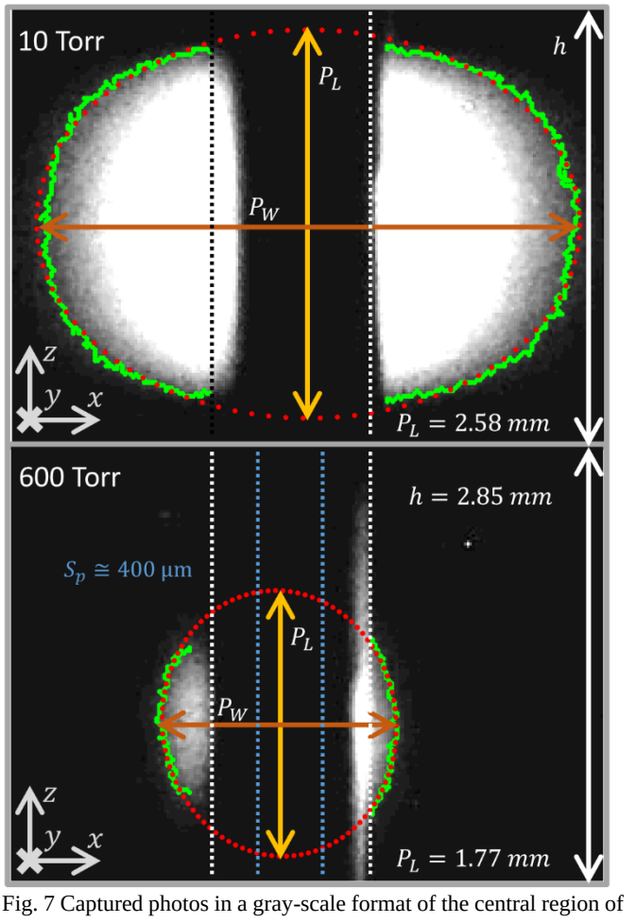

Fig. 7 Captured photos in a gray-scale format of the central region of the MMW photonic crystal, highlighting microplasma boundaries (green and red dotted lines) and the respective plasma length (P_L) and width (P_W), for a low and high pressure (10 and 600 Torr), at 1000 mW as forward power. The laser path ($S_p \cong 400\,\mu m$) is highlighted with a blue dotted line.

The optical depth and line-integrated density only provide an average measurement along the entire 2.8 mm optical path through the PhC vacancy. Both pressure and plasma power influence the actual plasma shape, and these variations may produce confusing measurement results due to changing path lengths through the plasma.

To estimate the average Ar($1s_5$) density, we record the length of the plasma P_L and then report the density as $N_i l / P_L$. Examples of the plasma shape are shown in Fig. 7 for the extrema in pressure examined here. The viewpoint in the

photographs is perpendicular to the laser path as highlighted with a blue dotted line ($S_p \cong 400$ µm). This view of the plasma is partially blocked by the 1 mm rods of the PhC (marked with vertical white lines).

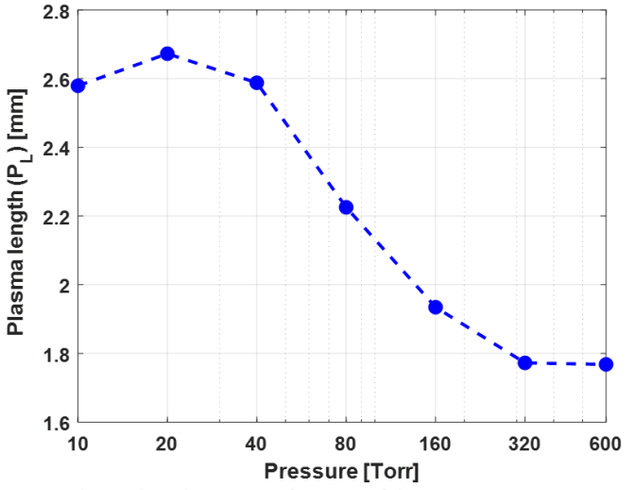

Fig. 8. Plasma length (P_L) as a function of the pressure, at 1000 mW forward power.

The rods obscure the center of the plasma and also scatter some plasma emissions to the camera. All images are captured with identical, fixed aperture and shutter speed to ensure consistency throughout the experimental parameter space. All images are converted to gray-scale and a gray-scale value is somewhat arbitrarily chosen as the edge of the plasma. This boundary is highlighted using green pixels in the images. This is a necessary approximation, so the reported density is merely the average over this estimated plasma length.

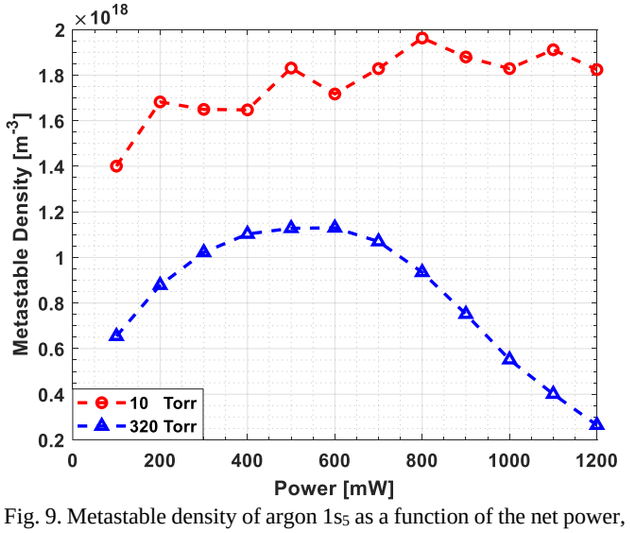

Fig. 9. Metastable density of argon $1s_5$ as a function of the net power, for a low (red curve) and high (blue curve) pressure (10 and 320 Torr).

The upper and lower boundaries of the plasma are always hidden by the PhC rods, so the plasma length is extracted by assuming that the shape is a general ellipsoid. The edge data are fitted in Matlab® using the function "fit_ellipse".

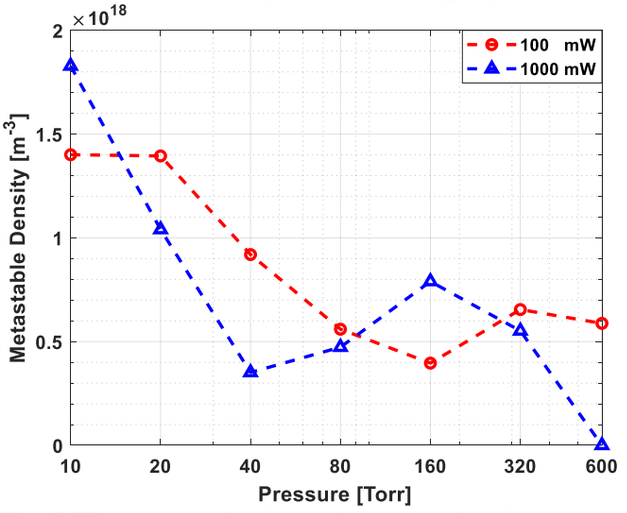

Fig. 10. Metastable density of argon $1s_5$ as a function of the pressure for a low (red curve) and high (blue curve) net power (100 mW and 1000 mW).

The red dotted line in Figure 7 shows the best-fit ellipsoid. The major and minor axes of the ellipse represent the plasma length (P_L) and width (P_W). Fig. 8 provides example dimensions for the plasma from 10-600 Torr (1000 mW). The plasma emission contracts from the limits imposed by the boundaries of the PhC (2.8 mm) to a free-floating length of 1.75 mm. Fig. 9 presents the volume-average metastable density as a function of power. The density is essentially averaged over a cylindrical volume defined by the cross-section of the laser path (400 µm in diameter) and the estimated plasma length. Typical metastable production within the PhC is the order of 10^{18} m^{-3}. Compared to the line-integrated density data, we see that the volume-averaged density has less variation after plasma constriction is included. The general trend, including depletion at high pressure, remains similar. The average density as a function of gas pressure is presented in Fig. 10. Two local minima in density remain and there is no detectable metastable density in the high power case at 600 Torr.

3.2 Absorption Line Broadening

One may estimate the gas temperature by considering the broadening of the absorption line [53] as shown in Fig. 4. The optical depth (kl vs $\Delta\lambda$) is a Voigt profile, which is the convolution of Gaussian and Lorentzian line profiles; the first due to the Doppler broadening and the second due to collisional and Stark broadening. We use a Voigt profile approximation to estimate the broadening for each profile, from which the gas temperature can be determined. In this

case the Stark broadening effect on argon can be ignored due to its negligible influence on the Lorentzian line profile. In the following subsections, we detail the theory for each profile and end by presenting the gas temperature results.

3.2.1 Doppler Broadening

The Gaussian profile is produced by the motion of the absorbing atoms. The lineshape for this profile is assumed to be generated by atoms with a Maxwellian distribution, where the FWHM [52] is given by:

$$\Delta\lambda_G = 7.16 \times 10^{-7} \lambda_0 \sqrt{\frac{T_g}{M}} \qquad (4)$$

Here $\Delta\lambda_G$ is in [m], M is the atomic mass of the absorbing Ar($1s_5$) atoms in [a.m.u], and T_g is the translational gas temperature in [K].

3.2.2 Collisional Broadening

This broadening is mostly produced by the collisions between the absorbing atoms, neutral gas atoms and other excited atoms, and its FWHM is given by:

$$\Delta\lambda_{Coll} = CN \qquad (5)$$

$\Delta\lambda_{Coll}$ is also in [m], C is the collisional broadening parameter in [$\mathrm{m \cdot m^3}$], and N is the neutral gas density in [$\mathrm{m^{-3}}$]. In some transition lines, such as that used in this work, C is dependent of gas temperature as follows:

$$\Delta\lambda_{Coll} = \left(\frac{C_0}{T_0^{0.3}}\right) T_g^{0.3} N \qquad (6)$$

Where C_0 is the collisional broadening parameter measured at a gas temperature, T_0. This parameter is estimated and compared with others in the literature [53]–[56] for this absorption line in Table II.

Table II. Comparison of the collisional broadening parameters C_0 for Ar absorption at 811.53 nm

C_0 [10^{-36} m · m^3] ($C_0/T_0^{0.3}$ [10^{-37} m · m^3 · K$^{-0.3}$])				
Tachibana [53]	**Lee** [54]	**Moussounda** [55]	**Vallee** [56]	**This work**
300 K	**300 K**	**2250 K**	**3900 K**	**340 K**
0.9 (1.69)	1.25 (2.26)	2.60(2.57)	1.91(1.60)	1.80(3.14)

In Table II values for C_0 are presented for different T_0. Using these literature values, the gas temperature was near or even below room temperature for our low pressure measurements. Therefore, we also experimentally estimated C_0. Using low pressure absorption data with small collisional broadening, we find the Doppler temperature $T_g \cong$ 340 K. Then, the pressure is slightly increased and the neutral gas density (N) is calculated ($N = P/kT_g$), to finally find the slope C_0 according to Equation (5).

Neglecting the small effects of the Stark broadening, the FWHM for the Lorentzian profile is given by:

$$\Delta\lambda_L = \Delta\lambda_{Coll} + \Delta\lambda_{Stark} \cong \Delta\lambda_{Coll} \qquad (7)$$

3.3 Voigt profile approximation and gas temperature T_g

The measured optical depth profiles were fitted with a Voigt profile using a least-squares error method in Matlab (fit2voigt.m). Examples of the Voigt profiles are plotted in Fig. 4. The Gaussian (σ) and Lorentzian (γ) components from the curve fitting procedure were converted to the FWHM of the absorption spectra using

$$\Delta\lambda_G = 2\sigma\sqrt{2\ln(2)} \qquad (8)$$

$$\Delta\lambda_L = 2\gamma \qquad (9)$$

Finally, T_{gL} was calculated through the Lorentzian profile by using Equation (6) and is presented in Fig. 11 and Fig. 12.

In Fig. 11, the argon gas temperature is shown as a function of the net power. At lower pressure, T_g is 300-500 K. The diffuse plasma cools on the PhC frame and expands horizontally with additional power, so the temperature remains low. As expected, at higher pressure, more frequent collisions heat the gas such that T_g was higher.

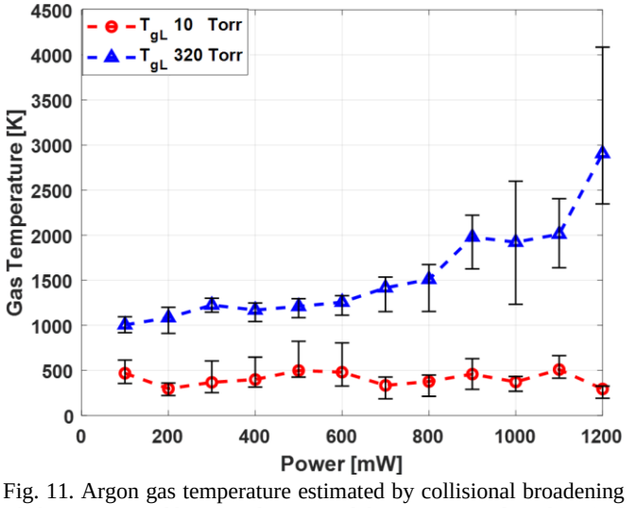

Fig. 11. Argon gas temperature estimated by collisional broadening of absorption profiles, as a function of the net power, for a low (red curve) and high (blue curve) pressure (10 and 320 Torr).

As the pressure and net power increase, the estimated error is more considerable. At higher pressure the collisional broadening of the optical depth increases, lowering the amplitude and decreasing the signal-to-noise ratio. This increases the uncertainty in the Voigt fit as reflected by the error bars.

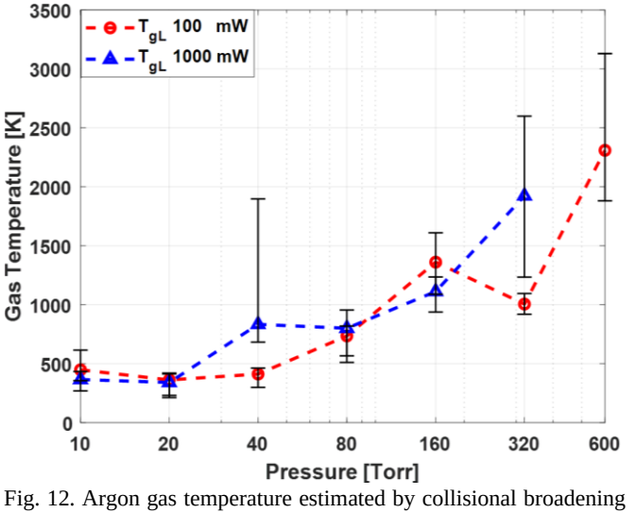

Fig. 12. Argon gas temperature estimated by collisional broadening of absorption profiles, as a function of the pressure, for a low (red curve) and high (blue curve) net power (100 mW and 1000 mW).

Fig. 12 shows the gas temperature as a function of the pressure. Similar to Fig. 11, an increasing evolution of the gas temperature can be observed as the pressure increases. The estimated error is greater for higher pressure and net power as before. The absence of absorption by $1s_5$ states for a pressure and net power of 600 Torr and 1000 mW, respectively, makes it impossible to estimate the gas temperature in the plasma for these values; however, following the curve trend, this temperature is expected to continue increasing.

4. Discussion

The photonic crystal provides a simple, scalable plasma-generating platform for extending microplasma generation into the THz band. Unlike microstrip and coaxial transmission lines, which become too lossy at extreme frequency, the PhC is known to remain functional into the optical wavelengths. The microplasma formed within a PhC is electrodelessly heated and floats in free space at higher pressures. Therefore, there are limited plasma-surface interactions to complicate the basic plasma physics, making the PhC an interesting reference cell for extreme frequency investigations.

This work can provide basic data for the development and validation of plasma models into the THz regime. Current models diverge in the predicted plasma electron density [42]–[44]. These experiments may help resolve the differences, but the models are typically one-dimensional in space. It is necessary to understand that the microplasma has a complex 3D structure, and this structure not only influences the model but also must be used to carefully interpret these data. Specifically, these data are extracted from the central 400 μm diameter core of the microplasma. Millimeter wave spectrometry of the microplasma by Kim and Hopwood [39] demonstrated that the microplasma has a small dense electron core (~200 μm) surrounded by a weak diffusion zone. Miura [57], investigating a microwave-driven microplasma, used Abel inversion to show that the central core has a high electron density ($>10^{20}$ m^{-3}), but those core electrons can (1) nearly fully dissociate diatomic molecules, and (2) nearly deplete the central core of metastable states - presumably by electron-impact ionization. The conceptual picture of a dense spheroid of electrons surrounded by a dense shell of metastable atoms also applies to the current data.

As electron density increases above 10^{20} m^{-3} with net wave power [37], the measured metastable density in the central core region decreases, somewhat counter-intuitively. It becomes too small to accurately measure near atmospheric pressure (1000 mW) but does become detectable again if the electron density (and temperature) decrease as power is reduced to 100 mW. Although the geometry of the PhC does not allow radial spatial resolution in experiments, we are likely observing the spheroid shell of metastable atoms expand outward with increasing power, leaving a void in the central measurement volume.

Previous reports of gas temperature on the same PhC microplasma indicate that the rotational temperature of the CH molecule increases from 400 to 900 K with power. The LD absorption technique reported here uses a more direct method because one does not need to assume that the translational and rotational gas temperatures are in equilibrium. Even so, the collisional broadening method indicates that the temperature reaches approximately 2000 K. This large discrepancy in the measured gas temperature is also related to the internal structure of the microplasma. The previous rotational temperature data was acquired by plasma emissions from a larger volume of the microplasma that includes the peripheral regions. Because the intense electron density in the core dissociates the CH molecule [58], the collected emission from the CH used for rotational temperature originates from the non-depleted periphery. This outer region is cooler than the core region that has been measured and reported here.

5. Conclusion

In this work, we have experimentally determined new characteristics of a 43 GHz microplasma operating from 10 – 600 Torr using 100 – 1200 mW of millimeter wave power. Using diode laser absorption, the central 400 μm core of the

microplasma is found to have an Ar($1s_5$) metastable density on the order of 10^{18} m^{-3} at low pressure (10 Torr). As the argon pressure is increased, however, the high electron density in the center of the microplasma ionizes the metastables. At 600 Torr, the metastable density is undetectable.

The gas temperature within the microplasma core is cool (300-500 K) at low pressure and low power. As expected, the gas temperature increases as the electron-neutral collision rate increases. At 300 Torr and higher, the translational gas temperature exceeds 2000 K in the center of the discharge. Optical emission measurements of the CH rotational temperature are approximately half this temperature, but the CH emissions are believed to emanate from the peripheral regions of the plasma. The diatomic molecules such as CH are depleted by dissociation in the electron-rich core and therefore have reduced emission. The absorption line shape, therefore, provides a more accurate indication of the core temperature. This method also becomes limited in utility as the metastable absorbers become depleted at the highest power levels reported here.

The characterization of the 43 GHz plasma aids our understanding of the basic physics of MMW microplasma generation. It is also hoped that these data can assist in the benchmarking and validation of models extending from the MMW to the THz regime. In the future, we will apply this diagnostic technique to a new, higher frequency microplasma operating at 94 GHz [59].

Acknowledgments

This work was supported by the U.S. Department of Energy under Award No. DE-SC0021249 and by the Air Force Office of Scientific Research (AFOSR) under Award No. FA9550-14-10317 through a Multi-University Research Initiative (MURI) Grant titled "Plasma-Based Reconfigurable Photonic Crystals and Metamaterials" with Dr. Mitat Birkan as the program manager. Special thanks to Mr. Scott MacCorkle for patiently and precisely machining the photonic crystal.

Data availability

The data that supports the findings of this study are available within the article [and its supplementary material].

References

[1] E. Yablonovitch, "Inhibited Spontaneous Emission in Solid-State Physics and Electronics," *Phys. Rev. Lett.*, vol. 58, no. 20, pp. 2059–2062, May 1987, doi: 10.1103/PhysRevLett.58.2059.

[2] S. John, "Strong localization of photons in certain disordered dielectric superlattices," *Phys. Rev. Lett.*, vol. 58, no. 23, pp. 2486–2489, Jun. 1987, doi: 10.1103/PhysRevLett.58.2486.

[3] S. John, "Electromagnetic Absorption in a Disordered Medium near a Photon Mobility Edge," *Phys. Rev. Lett.*, vol. 53, no. 22, pp. 2169–2172, Nov. 1984, doi: 10.1103/PhysRevLett.53.2169.

[4] P. W. Anderson, "Absence of Diffusion in Certain Random Lattices," *Phys. Rev.*, vol. 109, no. 5, pp. 1492–1505, Mar. 1958, doi: 10.1103/PhysRev.109.1492.

[5] J. M. Drake and A. Z. Genack, "Observation of nonclassical optical diffusion," *Phys. Rev. Lett.*, vol. 63, no. 3, pp. 259–262, Jul. 1989, doi: 10.1103/PhysRevLett.63.259.

[6] A. Z. Genack and N. Garcia, "Observation of photon localization in a three-dimensional disordered system," *Phys. Rev. Lett.*, vol. 66, no. 16, pp. 2064–2067, Apr. 1991, doi: 10.1103/PhysRevLett.66.2064.

[7] S. Noda, K. Tomoda, N. Yamamoto, and A. Chutinan, "Full Three-Dimensional Photonic Bandgap Crystals at Near-Infrared Wavelengths," *Science*, vol. 289, no. 5479, pp. 604–606, Jul. 2000, doi: 10.1126/science.289.5479.604.

[8] D. F. Sievenpiper, E. Yablonovitch, J. N. Winn, S. Fan, P. R. Villeneuve, and J. D. Joannopoulos, "3D Metallo-Dielectric Photonic Crystals with Strong Capacitive Coupling between Metallic Islands," *Phys. Rev. Lett.*, vol. 80, no. 13, pp. 2829–2832, Mar. 1998, doi: 10.1103/PhysRevLett.80.2829.

[9] E. Özbay, E. Michel, G. Tuttle, R. Biswas, M. Sigalas, and K. -M. Ho, "Micromachined millimeter-wave photonic band-gap crystals," *Appl. Phys. Lett.*, vol. 64, no. 16, pp. 2059–2061, Apr. 1994, doi: 10.1063/1.111736.

[10] J. Kitagawa, M. Kodama, S. Koya, Y. Nishifuji, D. Armand, and Y. Kadoya, "THz wave propagation in two-dimensional metallic photonic crystal with mechanically tunable photonic-bands," *Opt. Express*, vol. 20, no. 16, p. 17271, Jul. 2012, doi: 10.1364/OE.20.017271.

[11] J. D. Joannopoulos, Ed., *Photonic crystals: molding the flow of light*, 2nd ed. Princeton: Princeton University Press, 2008.

[12] J. D. Joannopoulos, P. R. Villeneuve, and S. Fan, "Photonic crystals: putting a new twist on light," *Nature*, vol. 386, no. 6621, pp. 143–149, Mar. 1997, doi: 10.1038/386143a0.

[13] S. Fan, P. R. Villeneuve, J. D. Joannopoulos, and E. F. Schubert, "High Extraction Efficiency of Spontaneous Emission from Slabs of Photonic Crystals," *Phys. Rev. Lett.*, vol. 78, no. 17, pp. 3294–3297, Apr. 1997, doi: 10.1103/PhysRevLett.78.3294.

[14] D. R. Smith, S. L. McCall, P. M. Platzman, R. Dalichaouch, N. Kroll, and S. Schultz, "Photonic band structure and defects in one and two dimensions," *J. Opt. Soc. Am. B*, vol. 10, no. 2, p. 314, Feb. 1993, doi: 10.1364/JOSAB.10.000314.

[15] W. M. Robertson, G. Arjavalingam, R. D. Meade, K. D. Brommer, A. M. Rappe, and J. D. Joannopoulos, "Measurement of photonic band structure in a two-dimensional periodic dielectric array," *Phys. Rev. Lett.*, vol. 68, no. 13, pp. 2023–2026, Mar. 1992, doi: 10.1103/PhysRevLett.68.2023.

[16] R. D. Meade, A. M. Rappe, K. D. Brommer, and J. D. Joannopoulos, "Nature of the photonic band gap: some insights from a field analysis," *J. Opt. Soc. Am. B*, vol. 10, no. 2, p. 328, Feb. 1993, doi: 10.1364/JOSAB.10.000328.

[17] S. Fan, J. D. Joannopoulos, J. N. Winn, A. Devenyi, J. C. Chen, and R. D. Meade, "Guided and defect modes in periodic dielectric waveguides," *J. Opt. Soc. Am. B*, vol. 12, no. 7, p. 1267, Jul. 1995, doi: 10.1364/JOSAB.12.001267.

[18] Y. Akahane, T. Asano, B.-S. Song, and S. Noda, "High-Q photonic nanocavity in a two-dimensional photonic crystal," *Nature*, vol. 425, no. 6961, pp. 944–947, Oct. 2003, doi: 10.1038/nature02063.

[19] A. Mekis, J. C. Chen, I. Kurland, S. Fan, P. R. Villeneuve, and J. D. Joannopoulos, "High Transmission through Sharp Bends in Photonic Crystal Waveguides," *Phys. Rev. Lett.*, vol. 77, no. 18, pp. 3787–3790, Oct. 1996, doi: 10.1103/PhysRevLett.77.3787.

[20] M. Moisan and J. Pelletier, *Physique des plasmas collisionnels: application aux décharges haute fréquence*. Les Ulis: EDP Sciences, 2006.

[21] M. A. Lieberman and A. J. Lichtenberg, *Principles of Plasma Discharges and Materials Processing: Lieberman/Plasma 2e*. Hoboken, NJ, USA: John Wiley & Sons, Inc., 2005. doi: 10.1002/0471724254.

[22] R. Navarro, L. Liard, and J. Sokoloff, "Effects of a low pressure plasma on a negative-permeability metamaterial," *Journal of Applied Physics*, vol. 126, no. 16, Art. no. 16, Oct. 2019, doi: 10.1063/1.5120479.

[23] H. Kim and J. Hopwood, "Wave Propagation in Composites of Plasma and Metamaterials with Negative Permittivity and Permeability," *Scientific Reports*, vol. 9, no. 1, Art. no. 1, Feb. 2019, doi: 10.1038/s41598-019-39923-7.

[24] F. Iza and J. Hopwood, "Split-ring resonator microplasma: microwave model, plasma impedance and power efficiency," *Plasma Sources Science and Technology*, vol. 14, no. 2, Art. no. 2, May 2005, doi: 10.1088/0963-0252/14/2/023.

[25] P. K. Singh, J. Hopwood, and S. Sonkusale, "Metamaterials for Remote Generation of Spatially Controllable Two Dimensional Array of Microplasma," *Scientific Reports*, vol. 4, p. 5964, Aug. 2014, doi: 10.1038/srep05964.

[26] H. Kim and J. Hopwood, "Plasma-enhanced metamaterials using microwave radiative power transfer," *Plasma Sources Science and Technology*, vol. 27, no. 9, Art. no. 9, Sep. 2018, doi: 10.1088/1361-6595/aadb64.

[27] Y. Nakamura and O. Sakai, "High-density microwave plasma source using negative-permeability metamaterial with tuned wave attenuation," *Japanese Journal of Applied Physics*, vol. 53, no. 3S2, Art. no. 3S2, Jan. 2014, doi: 10.7567/JJAP.53.03DB04.

[28] B. Wang and M. A. Cappelli, "A tunable microwave plasma photonic crystal filter," *Applied Physics Letters*, vol. 107, no. 17, Art. no. 17, Oct. 2015, doi: 10.1063/1.4934886.

[29] J. Lo, J. Sokoloff, Th. Callegari, and J. P. Boeuf, "Reconfigurable electromagnetic band gap device using plasma as a localized tunable defect," *Applied Physics Letters*, vol. 96, no. 25, Art. no. 25, Jun. 2010, doi: 10.1063/1.3454778.

[30] B. Wang and M. A. Cappelli, "A plasma photonic crystal bandgap device," *Appl. Phys. Lett.*, vol. 108, no. 16, p. 161101, Apr. 2016, doi: 10.1063/1.4946805.

[31] S. Parsons, J. Gregório, and J. Hopwood, "Microwave plasma formation within a 2D photonic crystal," *Plasma Sources Sci. Technol.*, vol. 26, no. 5, p. 055002, Mar. 2017, doi: 10.1088/1361-6595/aa62ed.

[32] J. Gregório, S. Parsons, and J. Hopwood, "Reconfigurable photonic crystal using self-initiated gas breakdown," *Plasma Sources Sci. Technol.*, vol. 26, no. 2, p. 02LT03, Jan. 2017, doi: 10.1088/1361-6595/26/2/02LT03.

[33] O. Sakai, T. Sakaguchi, and K. Tachibana, "Verification of a plasma photonic crystal for microwaves of millimeter wavelength range using two-dimensional array of columnar microplasmas," *Applied Physics Letters*, vol. 87, no. 24, Art. no. 24, Dec. 2005, doi: 10.1063/1.2147709.

[34] P. P. Sun, W. Chen, R. Zhang, Z. Liang, P. Braun, and J. G. Eden, "Student Excellence Award Finalist: Three Dimensional Microplasma/Metal/Dieletric Photonic Crystal : Dynamic Bandstop Filters," p. FT3.001, Jan. 2018.

[35] D. R. Biggs, A. Marcovati, and M. A. Cappelli, "Millimeter wave control using a plasma filled photonic crystal resonator," *J. Phys. D: Appl. Phys.*, vol. 52, no. 5, p. 055202, Jan. 2019, doi: 10.1088/1361-6463/aaee3d.

[36] S. G. Parsons and J. Hopwood, "Millimeter Wave Plasma Formation Within a 2D Photonic Crystal," *IEEE Electron Device Lett.*, vol. 38, no. 11, pp. 1602–1605, Nov. 2017, doi: 10.1109/LED.2017.2750486.

[37] H. Kim, S. Parsons, and J. Hopwood, "Spectroscopic diagnostics of continuous and transient microplasma formed in a millimeter wave photonic crystal," *Plasma Sources Sci. Technol.*, vol. 29, no. 4, p. 045001, Mar. 2020, doi: 10.1088/1361-6595/ab75a0.

[38] H. Kim and J. Hopwood, "Tunable millimeter wave photonic crystal for limiting high power pulses using weakly ionized steady state plasma," *Journal of Applied Physics*, vol. 128, no. 9, p. 093302, Sep. 2020, doi: 10.1063/5.0018252.

[39] H. Kim and J. Hopwood, "*In situ* millimeter wave spectroscopy of microplasma within a photonic crystal," *Journal of Applied Physics*, vol. 129, no. 3, p. 033301, Jan. 2021, doi: 10.1063/5.0032522.

[40] I. Adamovich *et al.*, "Plasma: at the frontier of scientific discovery," USDOE Office of Science (SC) (United States), Apr. 2017. doi: 10.2172/1615243.

[41] T. W. Crowe, W. L. Bishop, D. W. Porterfield, J. L. Hesler, and R. M. Weikle, "Opening the terahertz window with integrated diode circuits," *IEEE Journal of Solid-State Circuits*, vol. 40, no. 10, pp. 2104–2110, Oct. 2005, doi: 10.1109/JSSC.2005.854599.

[42] J. Gregório, A. R. Hoskinson, and J. Hopwood, "Modeling of microplasmas from GHz to THz," *Journal of Applied Physics*, vol. 118, no. 8, p. 083305, Aug. 2015, doi: 10.1063/1.4928468.

[43] D. Levko and L. L. Raja, "Microwave microplasma parameters at extremely high driving frequencies," *Physics of Plasmas*, vol. 26, no. 1, p. 014505, Jan. 2019, doi: 10.1063/1.5058065.

[44] A. Alamatsaz and A. Venkattraman, "A kinetic study of electron heating and plasma dynamics in microwave microplasmas," *Physics of Plasmas*, vol. 26, no. 1, p. 013512, Jan. 2019, doi: 10.1063/1.5082307.

[45] N. Sadeghi, "Molecular Spectroscopy Techniques Applied for Processing Plasma Diagnostics," *J. Plasma Fusion Res.*, vol. 80, no. 9, pp. 767–776, 2004, doi: 10.1585/jspf.80.767.

[46] S. G. Belostotskiy, V. M. Donnelly, D. J. Economou, and N. Sadeghi, "Spatially Resolved Measurements of Argon Metastable $(1{\rm s}_{5})$ Density in a High Pressure Microdischarge Using Diode Laser Absorption Spectroscopy," *IEEE Trans. Plasma Sci.*, vol. 37, no. 6, pp. 852–858, Jun. 2009, doi: 10.1109/TPS.2009.2015949.

[47] L. Latrasse, N. Sadeghi, A. Lacoste, A. Bès, and J. Pelletier, "Characterization of high density matrix microwave argon plasmas by laser absorption and electric probe diagnostics," *J. Phys. D: Appl. Phys.*, vol. 40, no. 17, pp. 5177–5186, Sep. 2007, doi: 10.1088/0022-3727/40/17/024.

[48] S. Hübner, N. Sadeghi, E. A. D. Carbone, and J. J. A. M. van der Mullen, "Density of atoms in Ar*($3p^5$ 4s) states and gas temperatures in an argon surfatron plasma measured by tunable laser spectroscopy," *Journal of Applied Physics*, vol. 113, no. 14, p. 143306, Apr. 2013, doi: 10.1063/1.4799152.

[49] N. Miura, J. Xue, and J. A. Hopwood, "Argon Microplasma Diagnostics by Diode Laser Absorption," *IEEE Trans. Plasma Sci.*, vol. 38, no. 9, pp. 2458–2464, Sep. 2010, doi: 10.1109/TPS.2010.2053854.

[50] N. Miura and J. Hopwood, "Spatially resolved argon microplasma diagnostics by diode laser

absorption," *J. Appl. Phys.*, vol. 109, no. 1, p. 013304, Jan. 2011, doi: 10.1063/1.3531557.

[51] A. I. Vyskrebentsev and Yu. P. Raizer, "A simple theory of breakdown of monatomic nonlight gases in fields of any frequency from low to optical," *J Appl Mech Tech Phys*, vol. 14, no. 1, pp. 32–38, Jan. 1973, doi: 10.1007/BF00850574.

[52] A. C. G. Mitchell and M. W. Zemansky, *Resonance Radiation and Excited Atoms*, 1st edition. Cambridge Eng.: Cambridge University Press, 1971.

[53] K. Tachibana, H. Harima, and Y. Urano, "Measurements of collisional broadening and the shift of argon spectral lines using a tunable diode laser," *J. Phys. B: At. Mol. Phys.*, vol. 15, no. 18, pp. 3169–3178, Sep. 1982, doi: 10.1088/0022-3700/15/18/013.

[54] C. S. Lee, D. M. Camm, and G. H. Copley, "Van der Waals broadening of argon absorption lines," *Journal of Quantitative Spectroscopy and Radiative Transfer*, vol. 15, no. 3, pp. 211–216, Mar. 1975, doi: 10.1016/0022-4073(75)90142-9.

[55] P. S. Moussounda and P. Ranson, "Pressure broadening of argon lines emitted by a high-pressure microwave discharge (Surfatron)," *J. Phys. B: At. Mol. Phys.*, vol. 20, no. 5, pp. 949–961, Mar. 1987, doi: 10.1088/0022-3700/20/5/015.

[56] O. Vallee, P. Ranson, and J. Chapelle, "Measurements of broadening of argon lines and oscillator strengths of resonance lines," *Journal of Quantitative Spectroscopy and Radiative Transfer*, vol. 18, no. 3, pp. 327–336, Sep. 1977, doi: 10.1016/0022-4073(77)90063-2.

[57] N. Miura and J. Hopwood, "Internal structure of 0.9 GHz microplasma," *J. Appl. Phys.*, vol. 109, no. 11, p. 113303, Jun. 2011, doi: 10.1063/1.3592269.

[58] N. Miura and J. Hopwood, "Instability control in microwave-frequency microplasma," *Eur. Phys. J. D*, vol. 66, no. 5, p. 143, May 2012, doi: 10.1140/epjd/e2012-20739-7.

[59] J. Hopwood, "94 GHz microplasma sustained by a photonic crystal," *Plasma Sources Sci. Technol.*, vol. 30, no. 11, p. 115013, Nov. 2021, doi: 10.1088/1361-6595/ac3213.

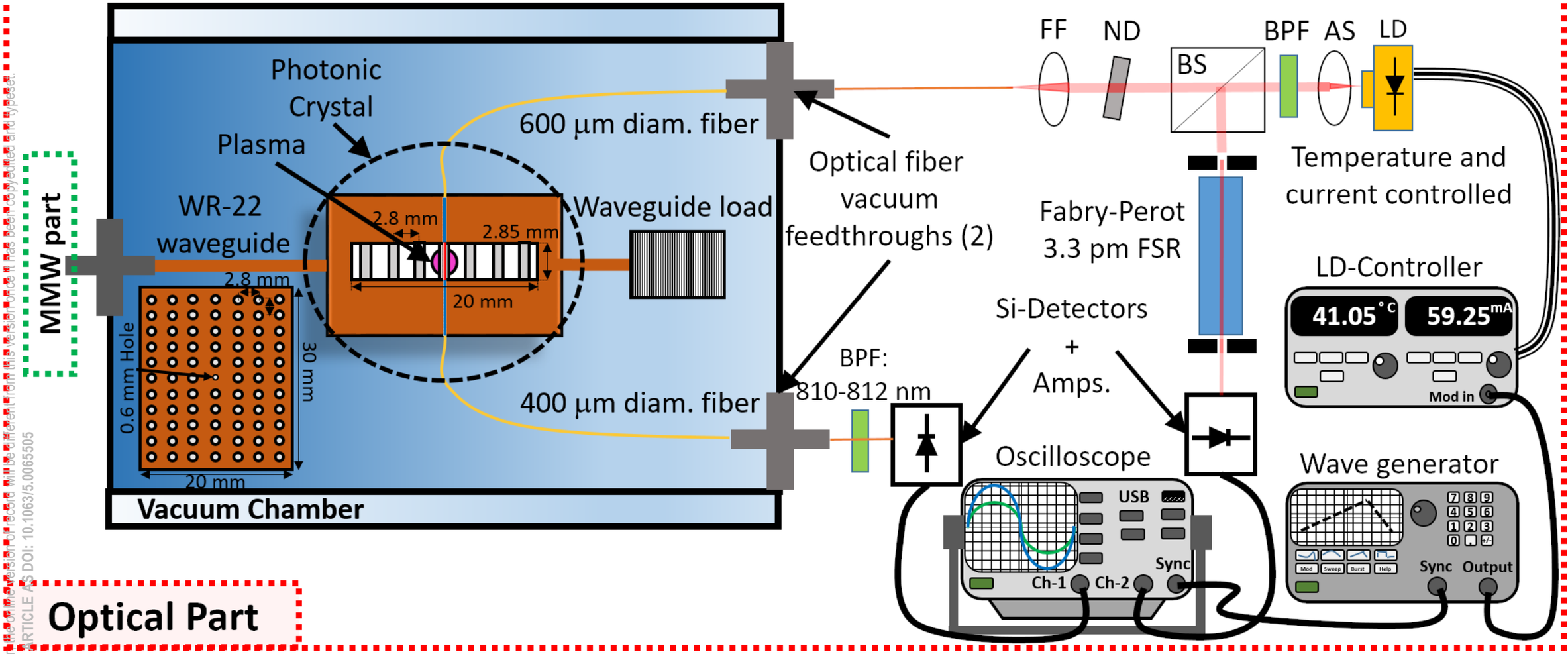

Optical Part

Journal of Applied Physics

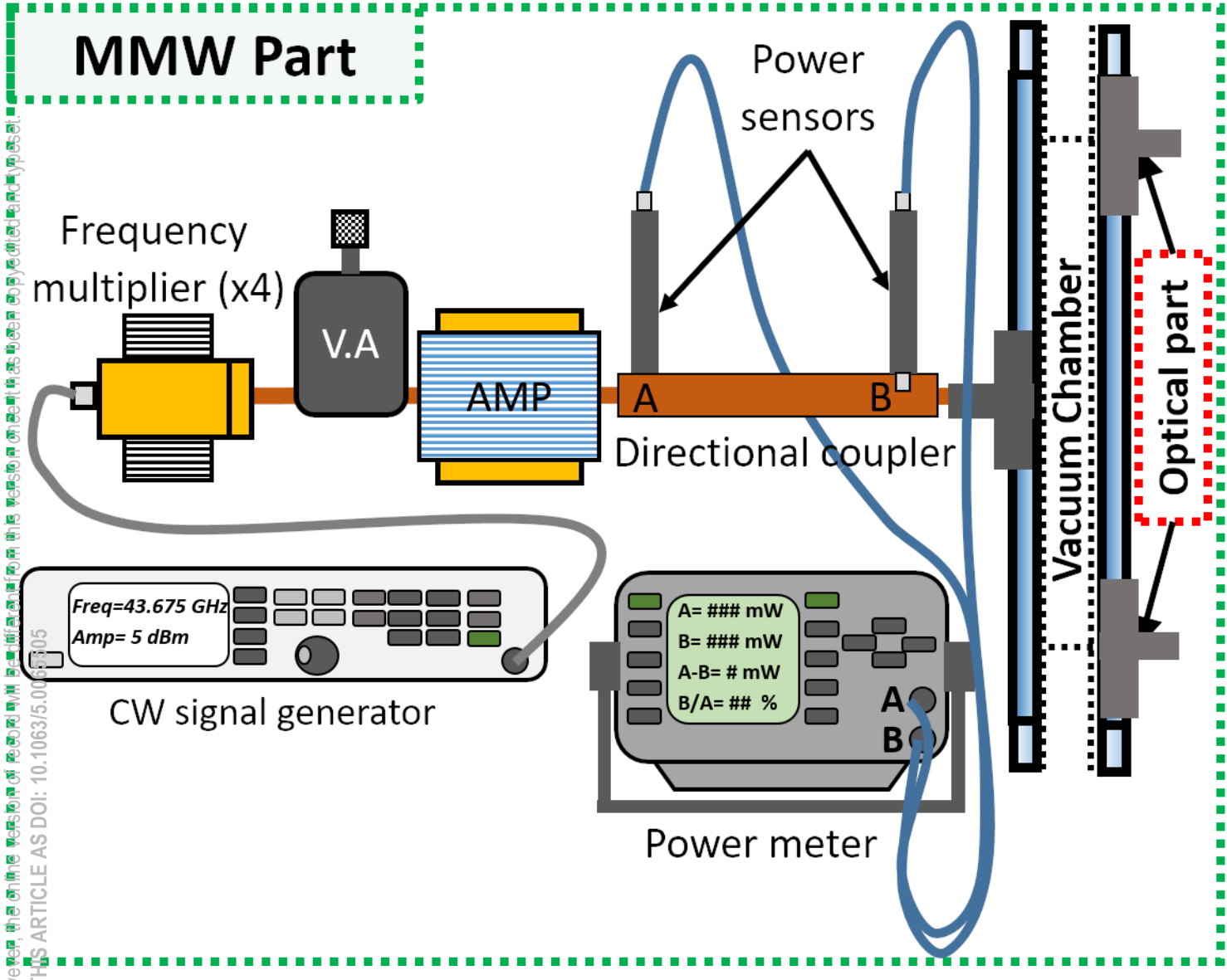

AIP Publishing

Journal of Applied Physics

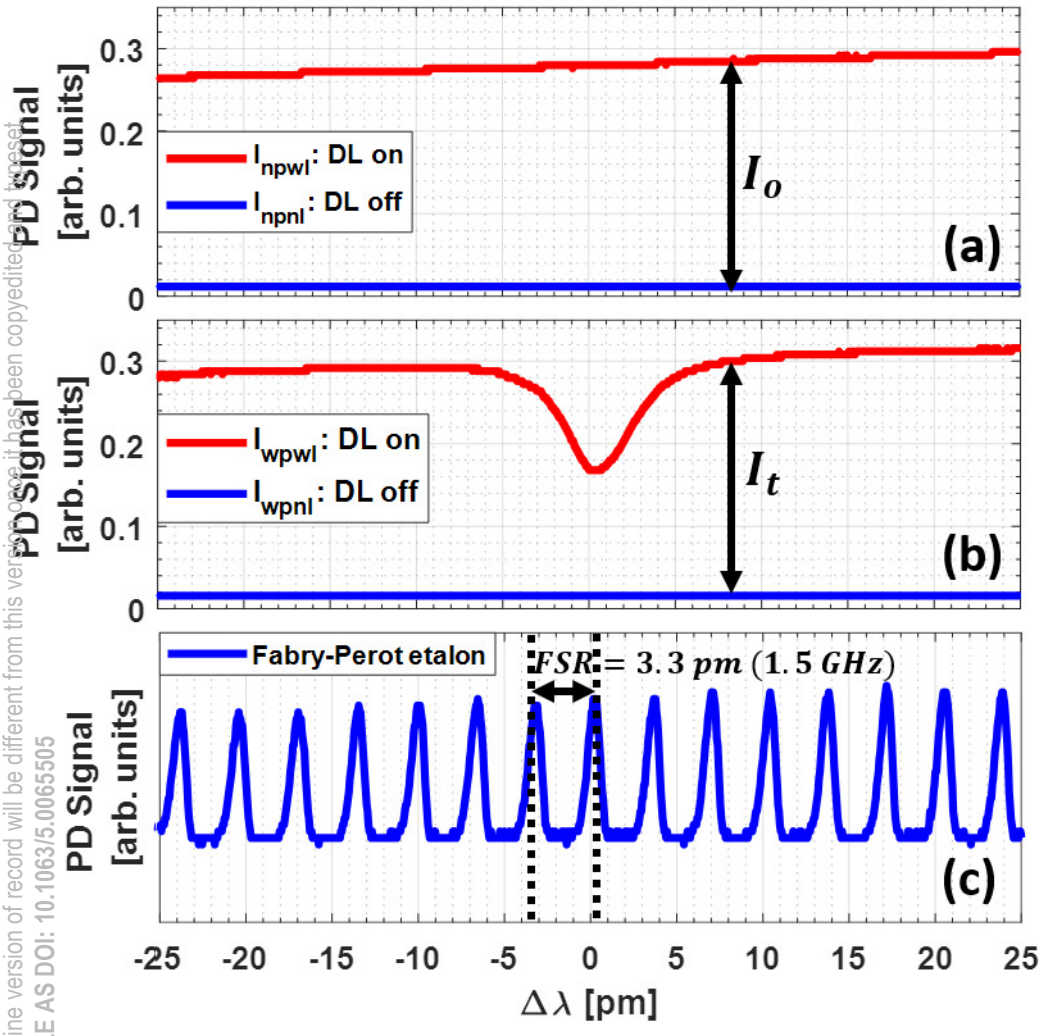

AIP Publishing

Journal of Applied Physics

PLEASE CITE THIS ARTICLE AS DOI: 10.1063/5.0065505

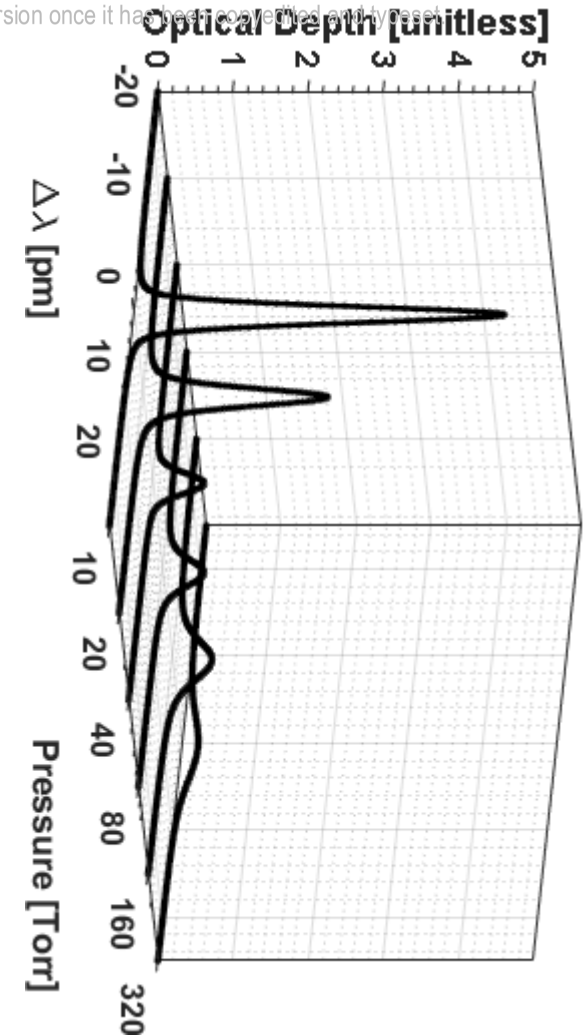

Journal of Applied Physics

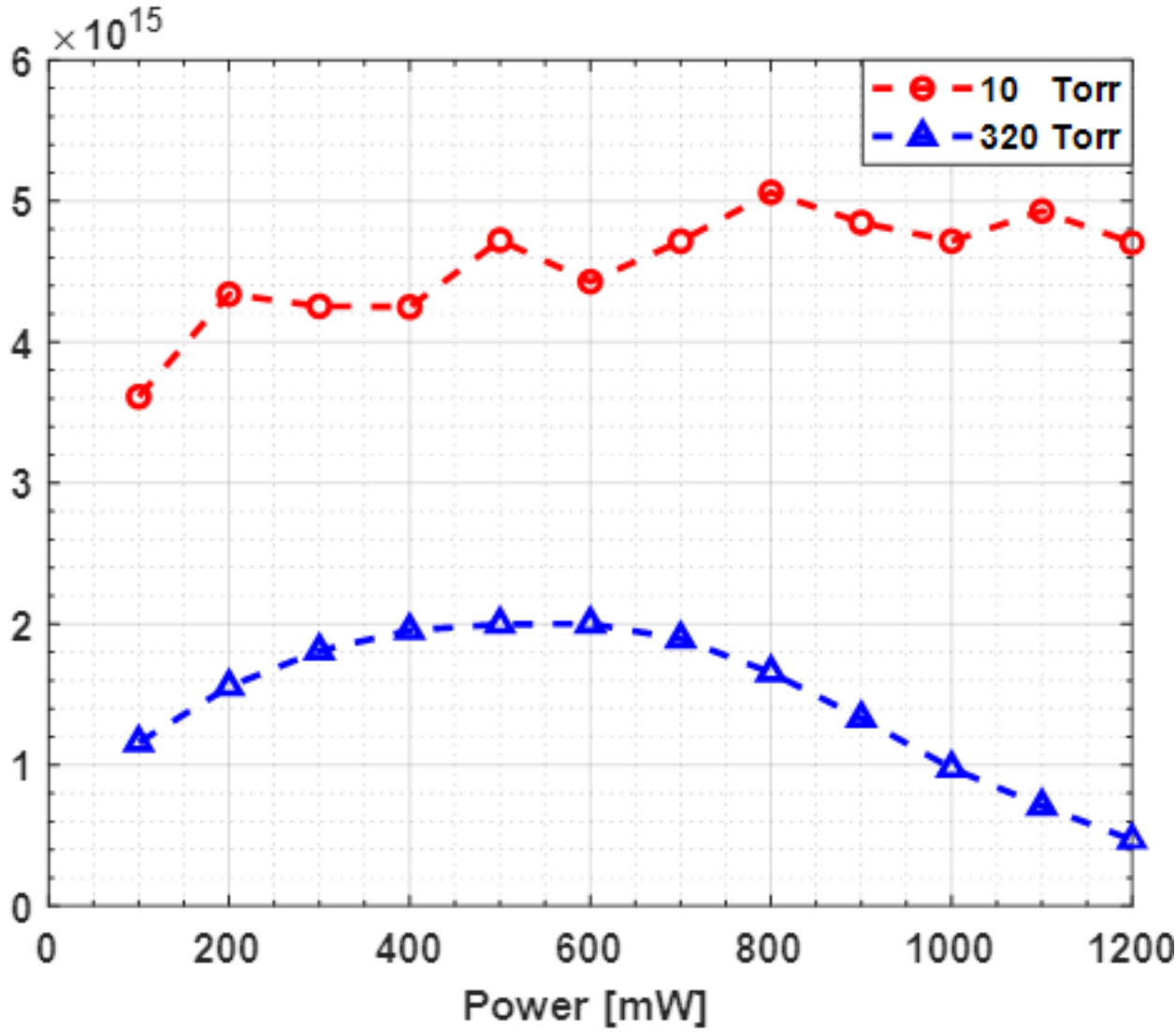

AIP Publishing

Journal of Applied Physics

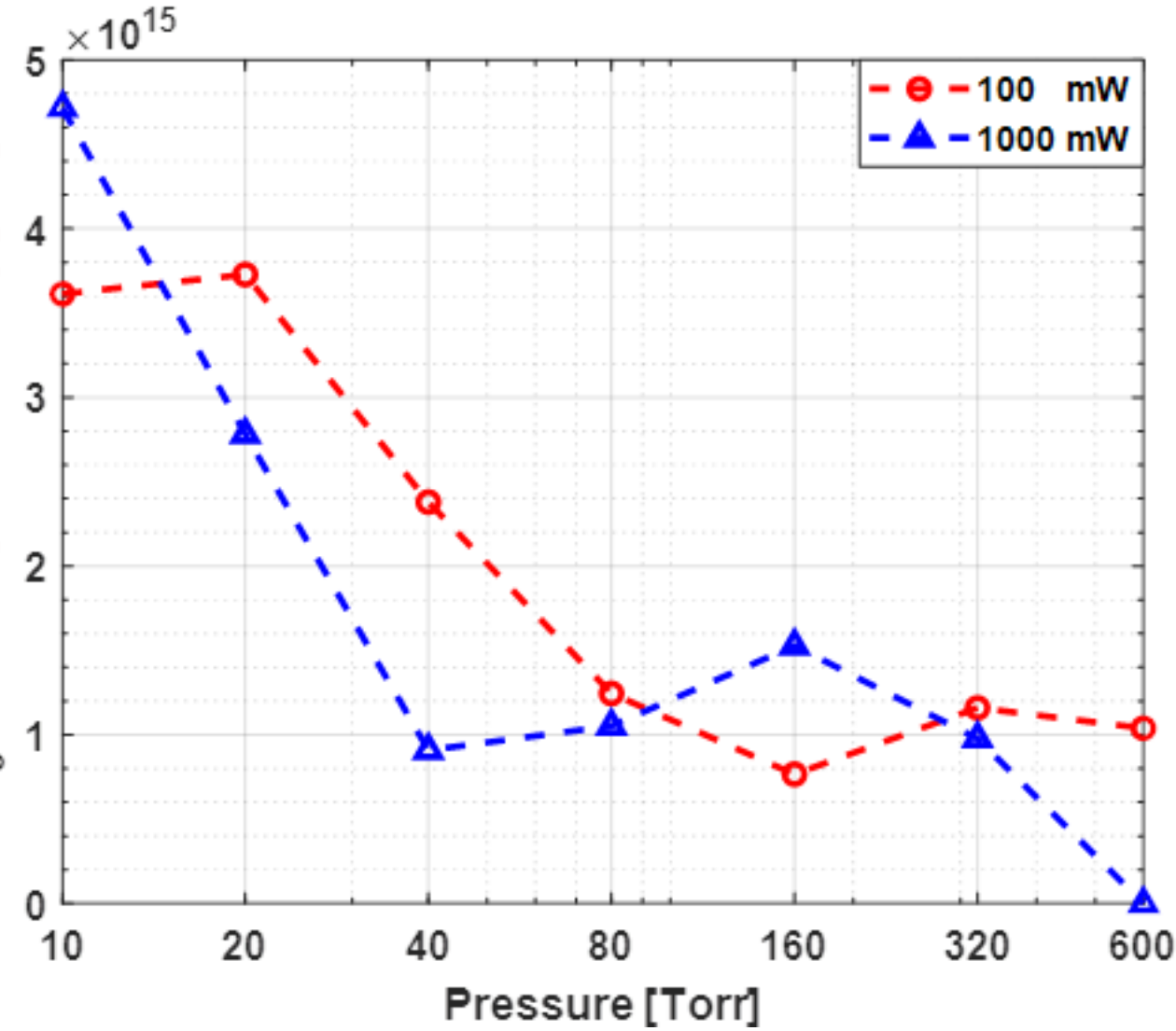

Journal of Applied Physics

PLEASE CITE THIS ARTICLE AS DOI: 10.1063/5.0065505

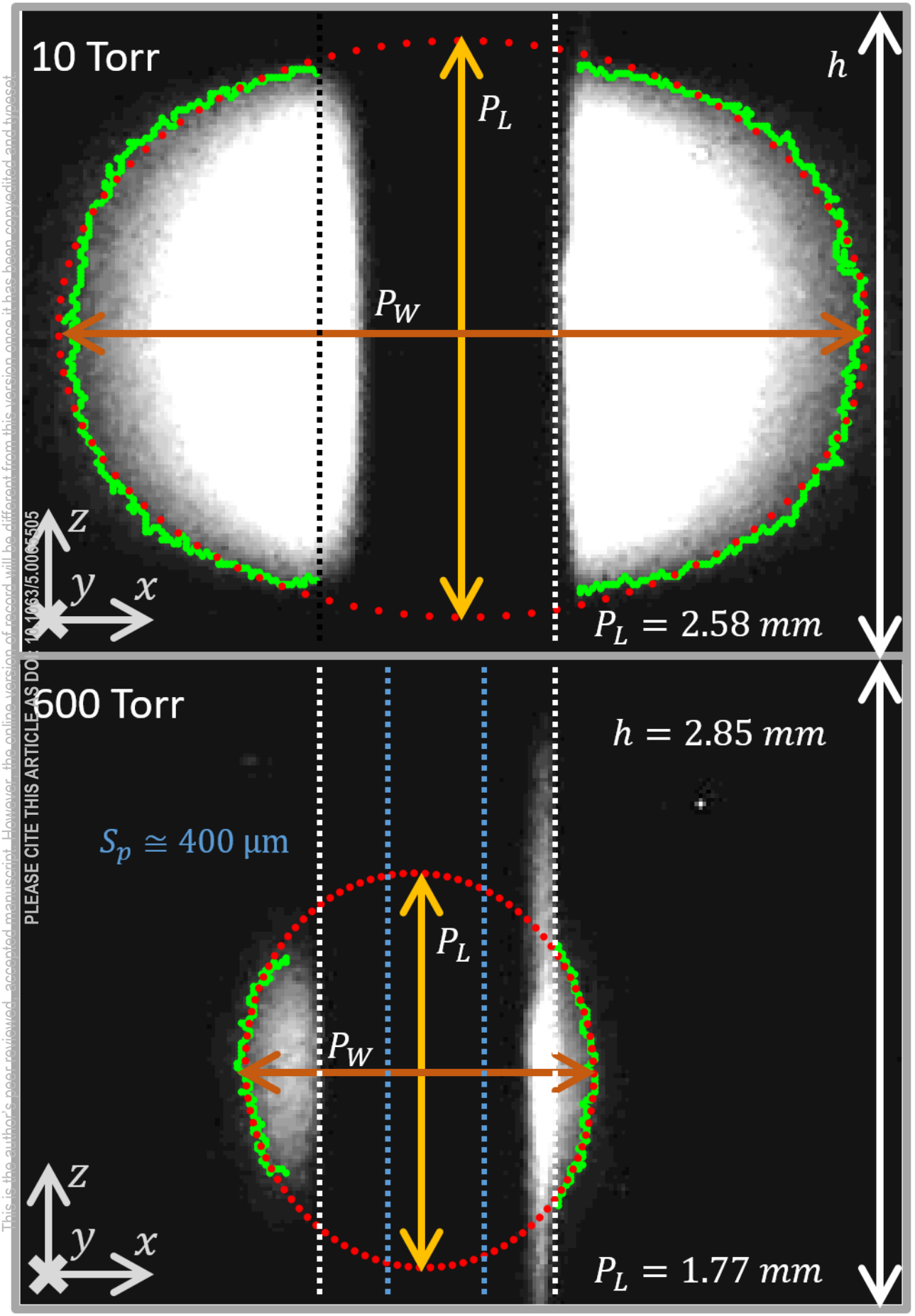

AIP Publishing

Journal of Applied Physics

PLEASE CITE THIS ARTICLE AS DOI: 10.1063/5.0065505

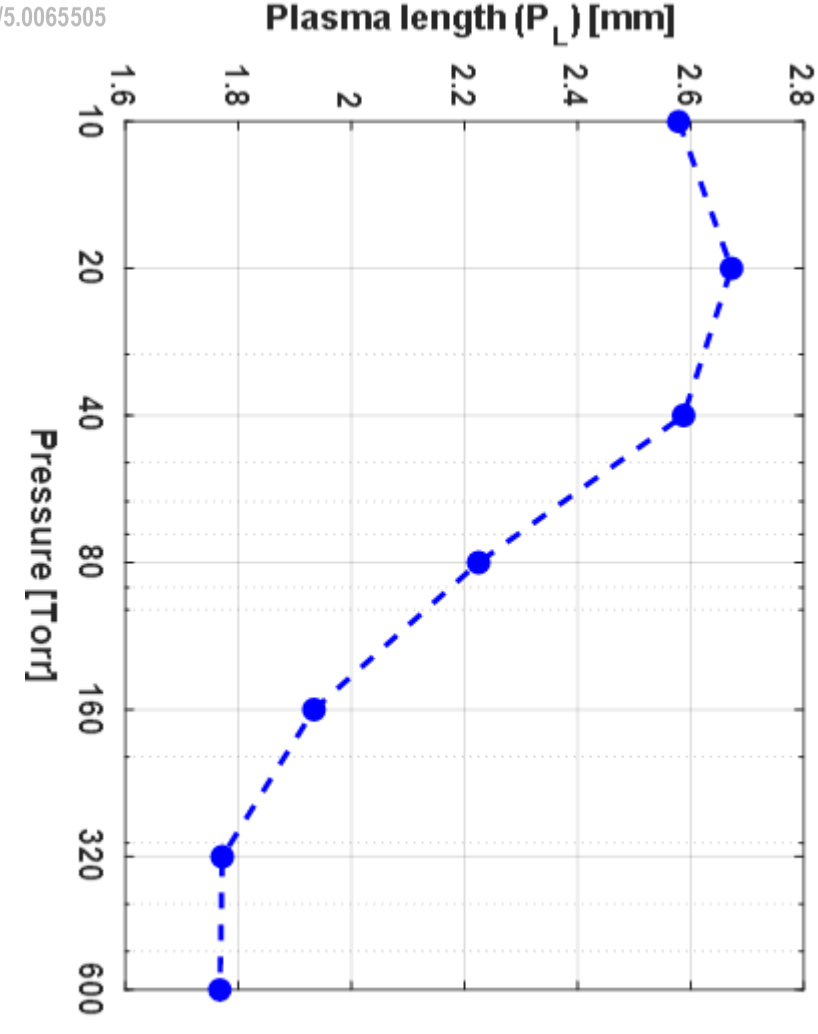

Journal of Applied Physics

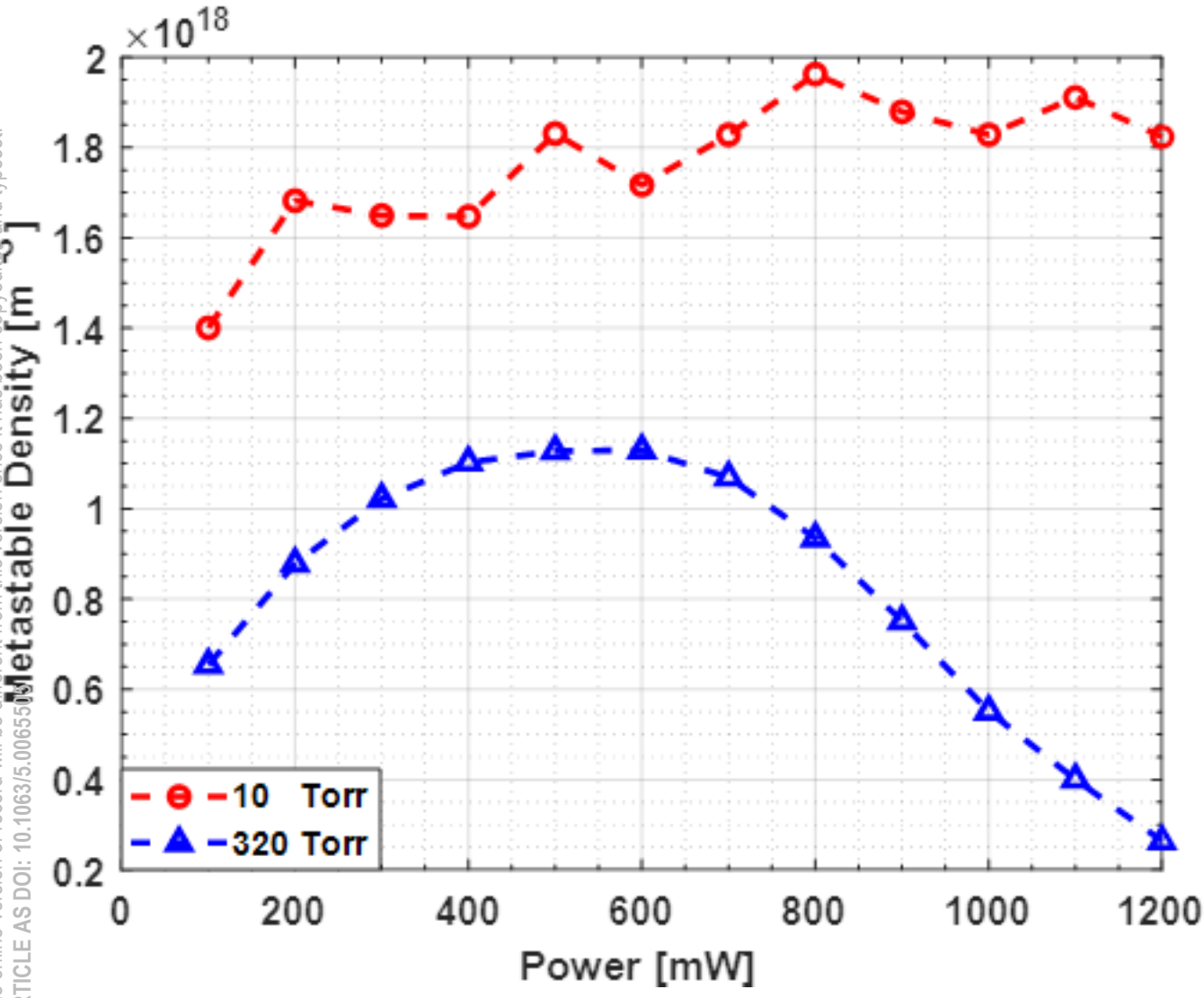

AIP Publishing

Journal of Applied Physics

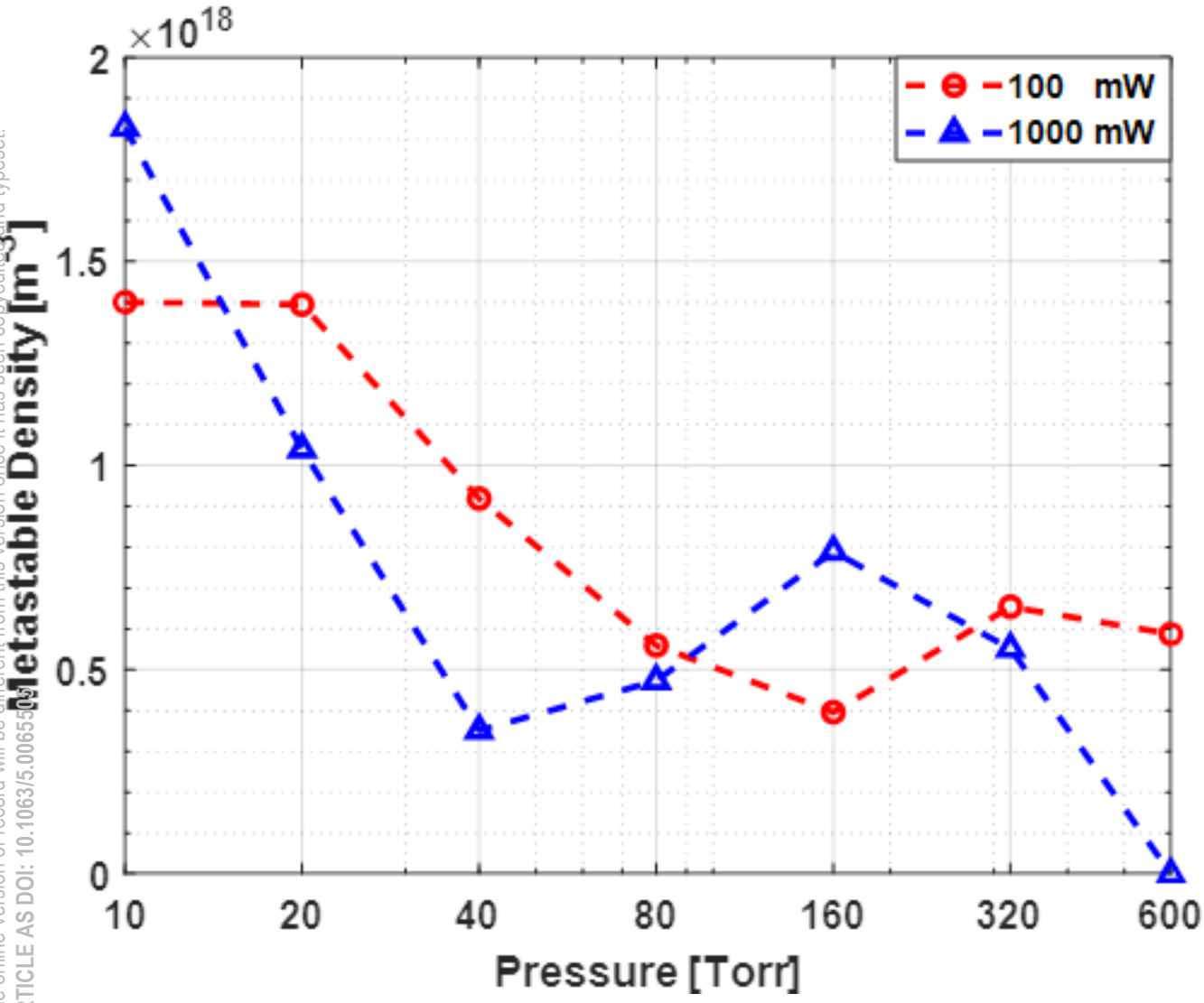

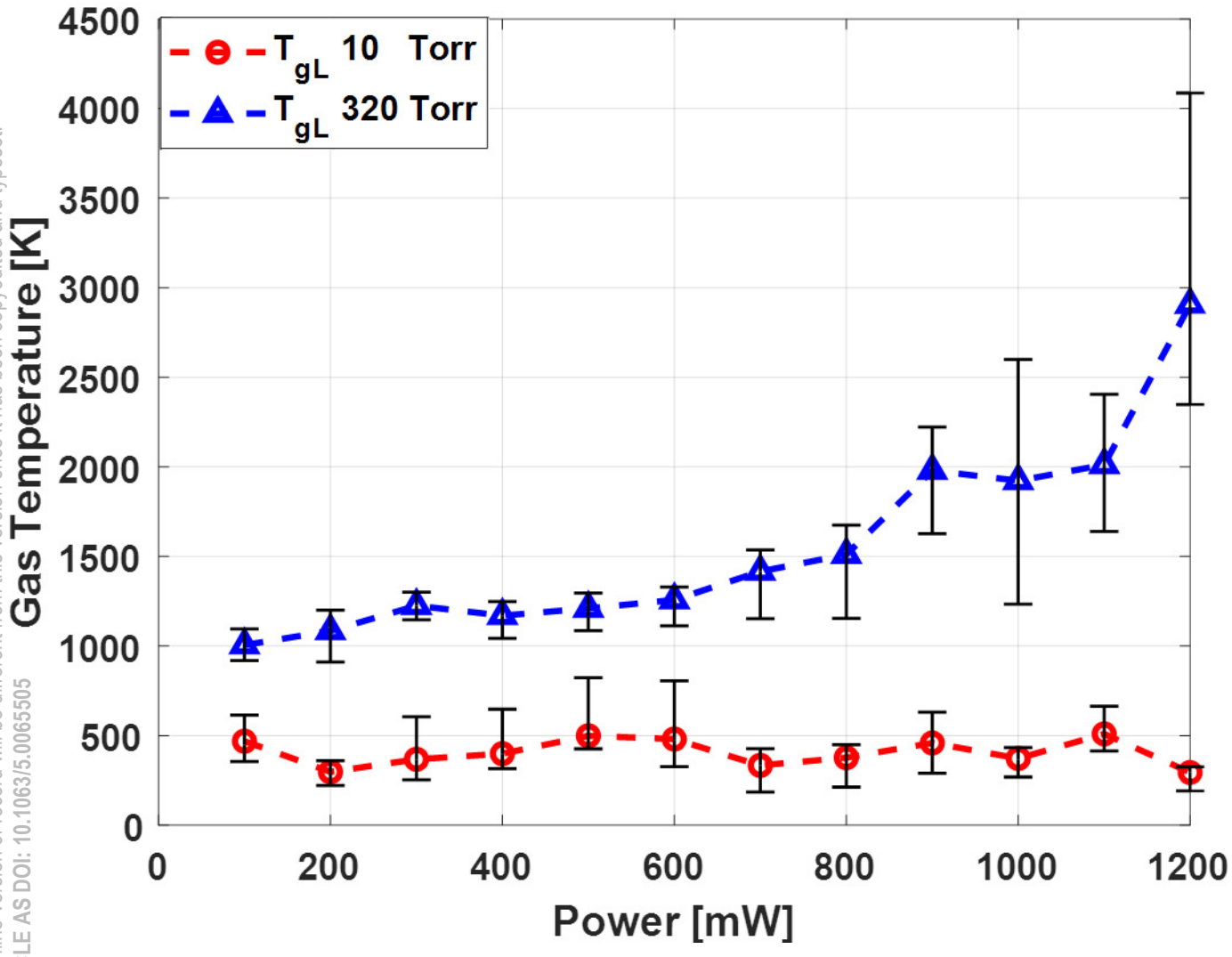

Journal of Applied Physics

AIP Publishing

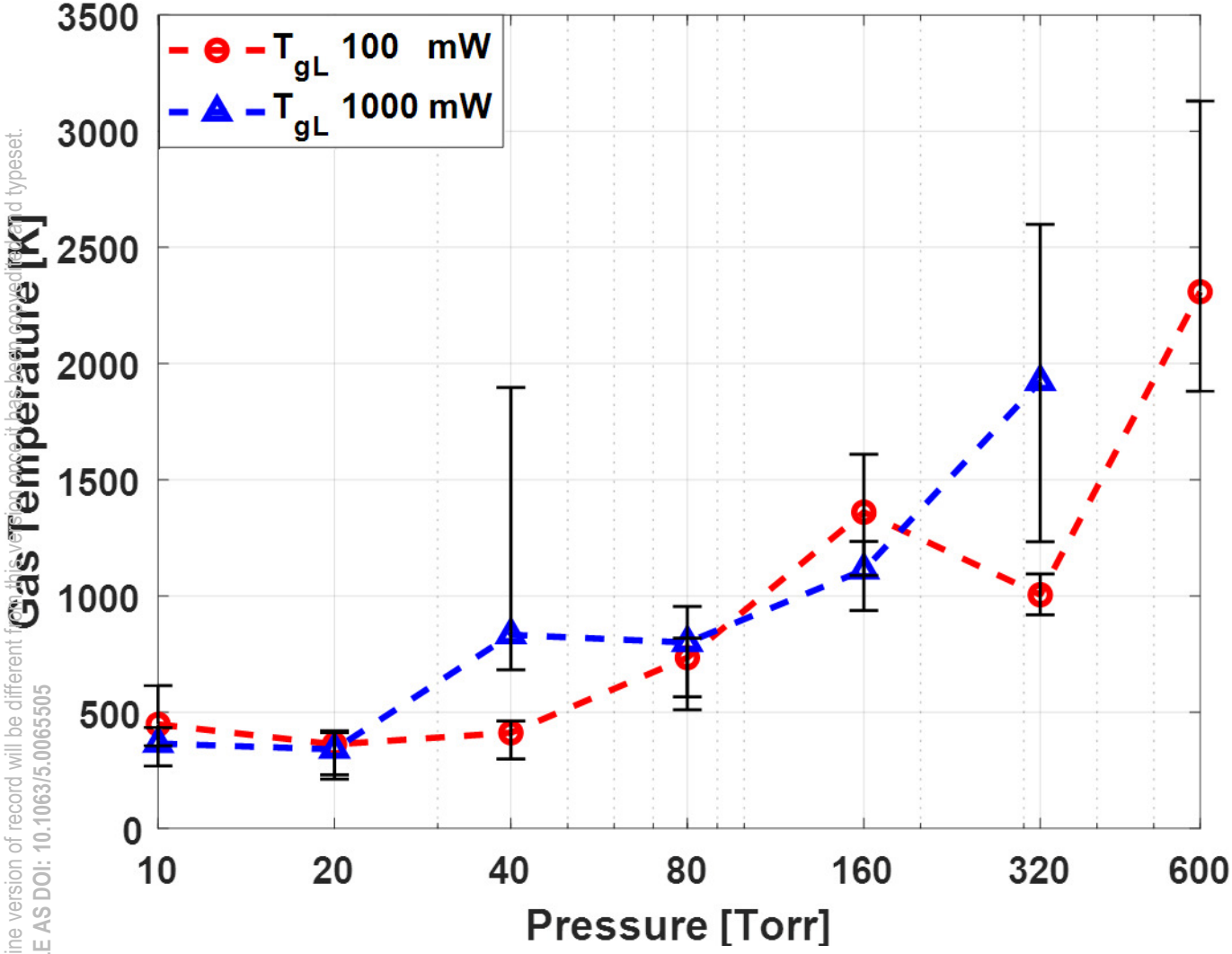

Journal of Applied Physics

AIP Publishing